Geophysical Research Letters

RESEARCH LETTER
10.1029/2020GL091207

Special Section:
The Ice, Cloud and land Elevation Satellite-2 (ICESat-2) on-orbit performance, data discoveries and early science

Buoyancy-Driven Flexure at the Front of Ross Ice Shelf, Antarctica, Observed With ICESat-2 Laser Altimetry

Maya K. Becker[1], Susan L. Howard[2], Helen A. Fricker[1], Laurie Padman[3], Cyrille Mosbeux[1], and Matthew R. Siegfried[4]

[1]Institute of Geophysics and Planetary Physics, Scripps Institution of Oceanography, University of California San Diego, La Jolla, CA, USA, [2]Earth & Space Research, Seattle, WA, USA, [3]Earth & Space Research, Corvallis, OR, USA, [4]Department of Geophysics, Colorado School of Mines, Golden, CO, USA

Abstract Mass loss from Antarctica's three largest ice shelves is dominated by calving, primarily of large tabular icebergs every few decades. Smaller, more frequent calving events also occur, but it is more difficult to detect them and quantify their contribution to total ice-shelf mass loss. We used surface elevation data from NASA's ICESat-2 laser altimeter to examine the structure of the Ross Ice Shelf front between October 2018 and July 2020. Profiles frequently show a depression a few meters deep about 200–800 m upstream of the front, with higher values on the eastern portion of the ice shelf. This structure results from bending due to buoyancy of a submerged ice bench generated by ice-front melting near the waterline when warm water is present in summer. These bending stresses may cause small-scale calving events whose frequency would change as summer sea ice and atmosphere–ocean heat exchanges vary over time.

Plain Language Summary Mass loss from Antarctica's floating ice shelves, which form as the ice sheet extends into the Southern Ocean, influences how quickly grounded ice flows into the ocean. Estimating future sea-level change from grounded-ice loss therefore requires understanding, and developing models for, the processes that affect ice shelves. We used measurements of surface height from NASA's recently launched ICESat-2 mission to explore one such process, the calving of small icebergs due to upper-ocean melting of the ice front. We focus on the large Ross Ice Shelf. This local melting leads to bending of the ice shelf that can be seen in ICESat-2 profiles that cross the ice front. The bending may also fracture the ice shelf to create small icebergs. We found that these surface structures are generally larger on the eastern portion of Ross Ice Shelf than on the western portion. We suggest that this pattern is due to differences in ice, ocean, and sea ice conditions that promote or impede the melting responsible for the ice-shelf bending. ICESat-2 will allow us to monitor changes in these small-scale structures and any associated calving events, which will provide clues about how ice shelves will change in the future.

Key Points:

- We used ICESat-2 laser altimetry to map prevalent rampart-moat (R-M) structures along the Ross Ice Shelf front
- R-M structures indicate a submerged buoyant bench seaward of the aerial ice front and ice stresses that may cause small-scale calving
- Along-front variation of R-M height differences provides insight into sensitivity to oceanic and glaciological conditions

Correspondence to:
M. K. Becker,
mayakbecker@gmail.com

Citation:
Becker, M. K., Howard, S. L., Fricker, H. A., Padman, L., Mosbeux, C., & Siegfried, M. R. (2021). Buoyancy-driven flexure at the front of Ross Ice Shelf, Antarctica, observed with ICESat-2 laser altimetry. *Geophysical Research Letters*, *48*, e2020GL091207. https://doi.org/10.1029/2020GL091207

Received 8 OCT 2020
Accepted 6 APR 2021

1. Introduction

Antarctica's floating ice shelves have a substantial effect on the rate of dynamic ice loss from the grounded Antarctic Ice Sheet (e.g., Thomas, 1979). For most ice shelves, a decrease in their mass reduces back stresses acting on the upstream glaciers and ice streams, resulting in acceleration of grounded ice into the ocean (e.g., Gudmundsson et al., 2019; Scambos et al., 2004; Smith, Fricker, Gardner, Medley, et al., 2020) and global sea-level rise (Nerem et al., 2018; Shepherd et al., 2018). In steady state, mass loss from an ice shelf, through basal melting and iceberg calving, balances inflow of grounded ice across the grounding line and net precipitation onto the ice shelf. In recent decades, however, ice-shelf mass losses integrated around Antarctica have exceeded gains (e.g., Adusumilli et al., 2020; Depoorter et al., 2013; Rignot et al., 2013).

For the largest ice shelves (Ross (Figure 1a), Filchner-Ronne, and Amery), which are underlain by cold water and currently near steady state, multidecadal mean mass loss through iceberg production is estimated to exceed loss through basal melting (Depoorter et al., 2013; Rignot et al., 2013). The calving flux for these ice shelves is dominated by intermittent production of large (tens of kilometers long) tabular icebergs every few decades (e.g., Fricker et al., 2002; Lazzara et al., 1999; Walker et al., 2021). The extent and timing of these calving events are controlled by the lateral extension of full-thickness rifts to the ice front. This process is usually treated as essentially glaciological, governed by ice-shelf stress balances (e.g., Joughin &

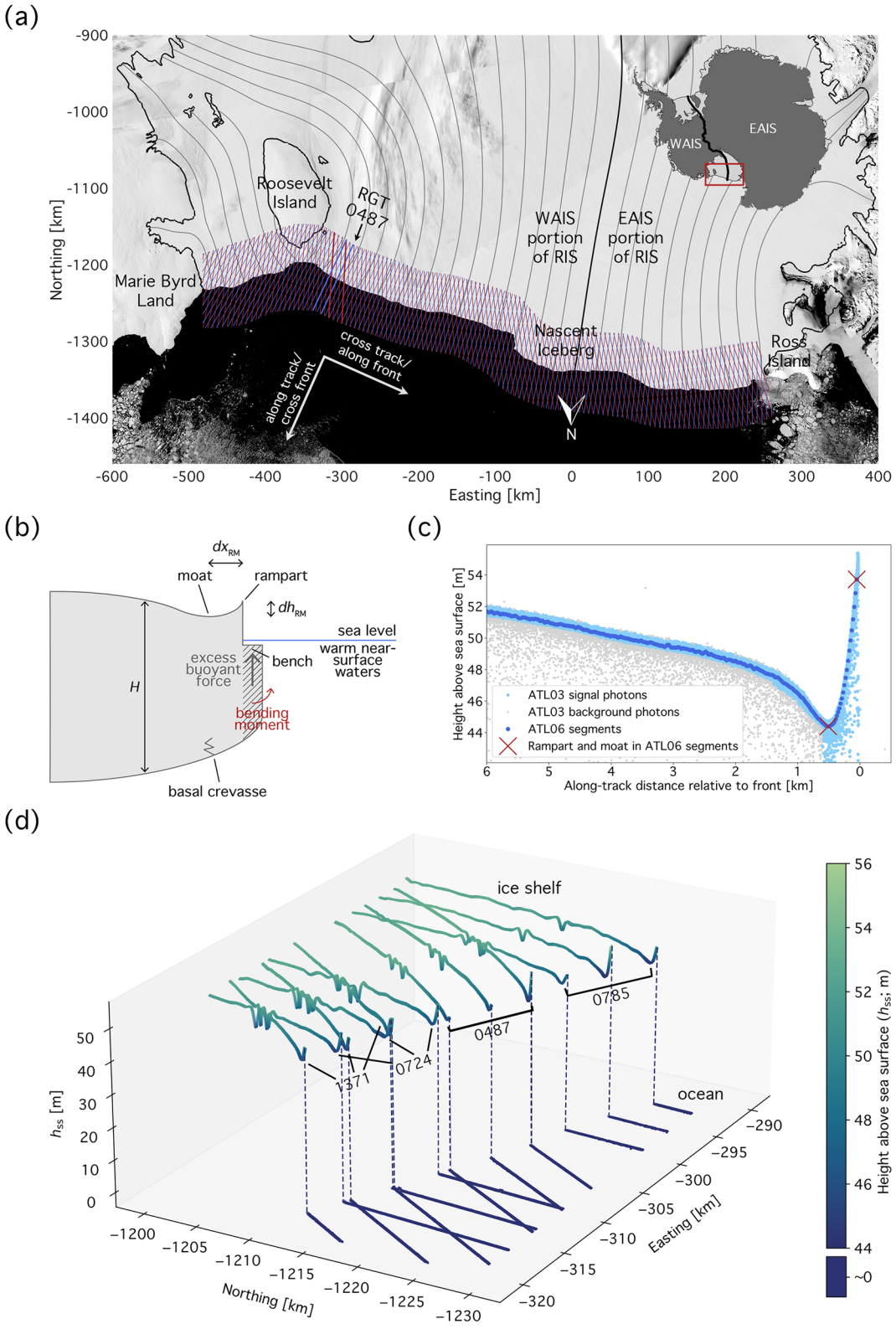
(a)
Northing [km]
Easting [km]
Roosevelt Island
RGT 0487
WAIS portion of RIS
EAIS portion of RIS
Marie Byrd Land
Nascent Iceberg
Ross Island
cross track/ along front
along track/ cross front
WAIS
EAIS
N
(b)
moat
rampart
sea level
warm near-surface waters
bench
excess buoyant force
bending moment
basal crevasse
H
(c)
Height above sea surface [m]
Along-track distance relative to front [km]
ATL03 signal photons
ATL03 background photons
ATL06 segments
Rampart and moat in ATL06 segments
(d)
ice shelf
ocean
0785
0487
0724
1371
Northing [km]
Easting [km]
Height above sea surface (h_{ss}; m)

MacAyeal, 2005), with the ocean making only an indirect contribution through ice-shelf thinning by melting (Liu et al., 2015) and possible contributions from tides, swell, and tsunamis (e.g., Bromirski et al., 2010; Brunt et al., 2011; MacAyeal et al., 2006). However, some mass loss can be driven directly by ice–ocean interactions at the front, including the more frequent production of relatively small "sliver-shaped" icebergs (described by Kristensen (1983) as <2 km long and having at least one horizontal dimension on the order of the ice thickness).

One potential small-scale calving mechanism involves the development of a buoyant subsurface ice "bench" (hatched area in Figure 1b) as warm near-surface water and surface-wave action cause the aerial portion of the ice front to collapse (e.g., Hughes, 2002; Orheim, 1987). The additional buoyancy bends the seaward ice edge upward, generating a surface "rampart" at the front and a depression (or "moat") upstream (Mosbeux et al., 2020; Scambos et al., 2005). The elevation difference (dh_{RM}) and horizontal distance (dx_{RM}) between the rampart and the center of the moat are, typically, a few meters and a few times the ice thickness (H), respectively (Scambos et al., 2005). Rampart-moat (R-M) structures have been observed at the edges of tabular icebergs as they drift into warmer upper-ocean water (Scambos et al., 2005, 2008; Wagner et al., 2014) and along the Ross Ice Shelf (RIS) front (Horgan et al., 2011; Mosbeux et al., 2020) where near-surface water warms in summer (Porter et al., 2019).

Mosbeux et al. (2020) applied an ice-shelf model to an idealized, constant-thickness ice shelf to quantify its flexural response to the buoyancy of the bench. An increase in buoyancy increases the associated internal ice stresses, which can lead to propagation of basal crevasses. If the stresses reach a critical value, the ice shelf will calve a relatively small, but full-thickness, iceberg along the crevasse. After the calving event, the new ice front will again be roughly vertical, with no bench. In that state, the dominant bending moment results from the difference in pressure between the ice shelf and the ocean along the ice front, which bends the upper edge seaward and downward (Reeh, 1968) by several meters to create a "berm" shape (Scambos et al., 2005). Berm structures are frequently found along ice fronts (e.g., Robin, 1979), where they can be reinforced by elevated rates of "mode-3" basal melting near the front (Horgan et al., 2011; Jacobs et al., 1992).

Until recently, we have lacked the ability to map surface elevation of Antarctica's extensive ice fronts at sufficiently high spatial resolution to fully resolve R-M structures. The 2018 launch of NASA's Ice, Cloud, and land Elevation Satellite-2 (ICESat-2) provides the first opportunity to overcome this observational limitation. Here, we demonstrate that ICESat-2 resolves R-M structures, map their presence along most of the RIS front, and examine along-front variability of R-M spatial scales. We then discuss potential environmental drivers and implications of this process as ocean conditions change.

2. ICESat-2 Over the RIS Front

2.1. ICESat-2 Mission

ICESat-2 was launched in September 2018 and began collecting scientific data in October 2018. The satellite carries the Advanced Topographic Laser Altimeter System (ATLAS), a photon-counting laser altimeter that transmits green (532 nm wavelength) light split into three pairs of beams (Markus et al., 2017). Each pair consists of a strong beam and a weak beam separated by 90 m; pairs are separated by 3.3 km on the ground during nominal performance. ATLAS pulses at 10 kHz, illuminating ~10.6–12 m footprints (Magruder

Figure 1. (a) Map showing the distribution of Ice, Cloud, and land Elevation Satellite-2 (ICESat-2) reference ground tracks (RGTs) near the Ross Ice Shelf (RIS) front (ascending in red and descending in blue) overlaid on a December 2, 2018, Moderate Resolution Imaging Spectroradiometer (MODIS) image downloaded from NASA Worldview. The Depoorter et al. (2013) ice-shelf mask is shown with a black line. Gray lines on the ice shelf show modern ice streamlines derived from Rignot et al. (2017) velocity fields, with the streamline delineating the boundary between ice originating from the West and East Antarctic ice sheets (WAIS and EAIS, respectively) in thicker black. Inset map (created using Antarctic Mapping Tools data; Greene et al., 2017) features the Mouginot et al. (2017) WAIS–EAIS boundary. (b) Schematic of ice-shelf bench (hatched area), R-M structure, and the conditions under which the bench forms. Three relevant R-M parameters, relative height (dh_{RM}), relative along-track distance (dx_{RM}), and near-front thickness (H), are indicated. (c) Height above instantaneous sea surface for Cycle 7 ICESat-2 ATL03 signal (light blue dots) and background (gray dots) photons, and ATL06 segments (dark blue dots) for gt3r (strong beam) for RGT 0487, which is labeled in (a). ATL06-derived rampart and moat locations are marked as red crosses. (d) ATL06 height above instantaneous sea surface for all beams for Cycle 7 repeats of, from east to west along the front, RGTs 1371 (June 24, 2020), 0724 (May 12, 2020), 0487 (April 27, 2020), and 0785 (May 16, 2020). Dashed lines connect the ice-shelf (left) side of the profiles to the ocean (right) side but do not represent real ATL06 data. The four RGTs shown in (d) are indicated in (a) by thicker lines compared to the other RGTs.

et al., 2020) every ~0.7 m along each of the six ground tracks (GTs). GTs are nominally centered on 1,387 reference ground tracks (RGTs), which extend to a latitude of 88° and are repeated once per 91-day cycle. ICESat-2 was off-pointed 1–4 km from its RGTs for the first two cycles (Smith, Fricker, Gardner, Medley, et al., 2020) but has been exactly following its RGTs over the polar regions since April 1, 2019.

2.2. Height Data

We used the ICESat-2 ATL06 Land Ice Height product (Smith et al., 2019), which provides estimated heights (relative to the WGS84 ellipsoid) derived from 40 m along-track data segments that overlap by 50%, yielding 20 m spacing. Over flat parts of the Antarctic Ice Sheet, ATL06 data have accuracy and precision of <3 cm and <9 cm, respectively (Brunt et al., 2019). We used data from all six GTs per RGT. We examined Release 003 ATL06 data (Smith, Fricker, Gardner, Siegfried, et al., 2020) across the RIS front region from Cycle 1 to midway through Cycle 8 (July 16, 2020). We used the Python *icepyx* library (Scheick et al., 2019) to download a spatially subsetted data set of ATL06 files from the National Snow and Ice Data Center (NSIDC). The bounding box we applied, which spanned 77°S to 78.9°S and 163.5°E to 157.5°W, encompasses the entire RIS front.

For specific GTs, we also retrieved ATL03 Global Geolocated Photon Data files (Neumann et al., 2019) that provide estimates for latitude, longitude, and height relative to the WGS84 ellipsoid for all photons detected by ATLAS. We downloaded these profiles from NSIDC (Neumann et al., 2020) and used them to assess how well the ATL06 product resolves R-M structures (Section 3.1).

2.3. Ice-Front and R-M Detection

We automated detection of the ice front, R-M structures, and measurements of R-M spatial scales from ATL06 data using the following analysis steps:

1. *GT selection:* We used an ice-shelf mask (Depoorter et al., 2013) to select GTs that crossed the RIS front between Marie Byrd Land and the eastern tip of Ross Island (Figure 1a).
2. *GT filtering:* We removed GT segments with known data-quality issues, keeping only data for which the *atl06_quality_summary* flag equals 0.
3. *Height referencing and correction:* We converted all ellipsoidal height data (*h_li*) to height relative to the instantaneous sea surface by referencing them to the EGM2008 geoid (*geoid_h*, provided in the ATL06 product) and correcting for ocean tides (*tide_ocean*), inverted barometer effects (*dac*), and mean dynamic topography (*mdt*), using $h_{ss} = h\_li - geoid\_h - tide\_ocean - dac - mdt$. We obtained the values for *tide_ocean* and *dac* from the GOT4.8 model and MOG2D dynamic atmosphere correction values provided in the ATL06 product; we applied a constant value of –1.4 m for *mdt* (Andersen et al., 2015). We then removed outliers ($h_{ss} < -5$ m or $h_{ss} > 100$ m).
4. *Front detection:* Our front-detection algorithm scans GT profiles from the ocean to the ice shelf. We interpreted segments with $h_{ss} < 2$ m as the ocean surface; we selected this threshold to allow for the presence of snow-covered sea ice and uncertainties in the geophysical corrections. For each GT, the algorithm steps landward from the most seaward ocean point until it detects a height increase of 10–100 m over less than 80 m distance along track, where the starting point of the jump is an ocean point. The algorithm identifies the ice front as the location of the first point on the high side of the jump. It occasionally located the ice front at the northern edges of small icebergs in the Ross Sea, in regions of near-front rifting (e.g., seaward of Roosevelt Island), and on the ice shelf when ATL06 data are missing over the true ice front and the surface within a rift has $h_{ss} < 2$ m. We manually removed tracks where the detected ice front was clearly inconsistent with the full data set and nearly contemporaneous MODIS imagery.
5. *R-M detection:* For all ice-front segments, we defined the rampart surface height (h_R) as the highest point within 100 m of the front. This was usually the first ATL06 value on the ice shelf; however, sometimes the ice front in the ATL06 profile included one or more lower points resulting from the overlapping averaged segments or true structure on the aerial portion of the ice face. Moving landward, we then searched in the GT profile for elevations lower than h_R that were less than 2 km (along track) from the front; this threshold is based on the expected location of moats within a few ice thicknesses of the front (Mosbeux et al., 2020; Scambos et al., 2005) and the orientation of RGTs being roughly orthogonal to the front for

RIS (Figure 1a). If successful, we recorded the lowest point of the first detected depression as the moat with height h_M.

6. *R-M quantification:* For each GT profile that showed an R-M structure, we computed two parameters to define its geometry: dh_{RM} (= $h_R - h_M$) and dx_{RM} as the difference in height and along-track distance, respectively, between the rampart and the center of the moat (Figures 1b–1c).

2.4. Estimation of Ice Thickness

We estimated ice thickness (H) from ATL06-derived values of h_{ss} ~3 km upstream (along track) of the rampart, which for almost all RGTs used in this study (Figure 1a) is upstream of the expected zone of R-M flexure (Mosbeux et al., 2020; Figures 1b–1d). We converted h_{ss} to ice-equivalent thickness (H_{eq}) by assuming hydrostatic equilibrium, ice density of 917 kg m^{-3}, seawater density of 1028 kg m^{-3}, and firn air content (H_{fac}) derived from GSFC-FDM v1 simulations (updated from those performed in Smith, Fricker, Gardner, Medley, et al., 2020). We then computed H as the sum of H_{eq} and H_{fac}.

3. Results

In our region of interest, there were 8,191 GTs that crossed the RIS front. We were unable to identify the ice front for 3,953 of these. Clouds (identified with the ATL06 *cloud_flg_atm* parameter) were responsible for most (3,726) of the failed front detections, whereas our algorithm could not detect the front in 227 GT profiles. Of the 4,238 GT profiles with detected fronts, 348 occurred seaward of Roosevelt Island or on icebergs in the Ross Sea. We detected R-M structures (step 5 above) along 2,893 of the remaining 3,890 profiles (~74%). Thus, 997 (~26%) of these GT profiles exhibit a monotonically increasing surface profile, or berm structure, within 2 km of the detected front; this arises from a combination of pressure imbalance at the ice front, mode-3 basal melting, and ice spreading. We report only the results of step 5 for the GT profiles for which we could compute a physical H, that is, that also contained high-quality data outside of rifts ~3 km upstream of the detected rampart. There were 2,826 GT profiles (~73% of the 3,890 profiles described above) for 221 RGTs that satisfied this criterion.

3.1. ICESat-2 Resolution of Rampart-Moat Structures

The profiles of ATL03 signal photons (see example in Figure 1c) reveal the ice front and R-M structures; however, quantifying surface heights and rampart and moat locations requires assumptions about the near-surface photon distribution and consideration of uncertainties in geolocation of individual photons. The ATL06 algorithm applies additional photon filters, instrumental corrections, and photon scattering statistics to retrieve ice-surface height from geolocated photons (Smith et al., 2019). This allows us to identify the along-track locations of the rampart and moat to an accuracy of 20 m and quantify the vertical and horizontal scales of the R-M structure, with minimal reduction in dh_{RM} relative to the value we would obtain from ATL03 signal photons. We conclude that ATL06 is well suited to our application of analyzing R-M structures.

3.2. Along-Front Variability of Rampart-Moat Characteristics

The multi-beam sampling and RGT spacing of ICESat-2 over RIS provide along-front sampling of ~1–3 km during a single cycle (Figure 1d). Derived R-M parameters are consistent between the weak and strong beam GT profiles that are 90 m apart; however, we sometimes observed large variability between beam pairs (3.3 km apart) for the same RGT and between RGTs. For example, for the Cycle 7 repeat of RGT 0487, beams gt3l (weak) and gt3r (strong) showed an R-M structure with $dh_{RM} \approx 9.5$ m, whereas the other two beam pairs (~3.3 and ~6.6 km away) showed R-M structures with $dh_{RM} \approx 1$–2 m.

We evaluated the statistics of dh_{RM} and dx_{RM} for all available ICESat-2 cycles for seven regions along the ice front (Figure 2a), chosen to approximate the regions used by Horgan et al. (2011) in their estimation of mode-3 basal melt rates but adjusted to match pronounced streaklines representing major suture zones between distinct ice flow units. Broadly speaking, the values of both dh_{RM} and dx_{RM} (Figures 2b–2e) are larger on the eastern portion of the front (regions 1–4) than on the western portion (regions 5–7). On the

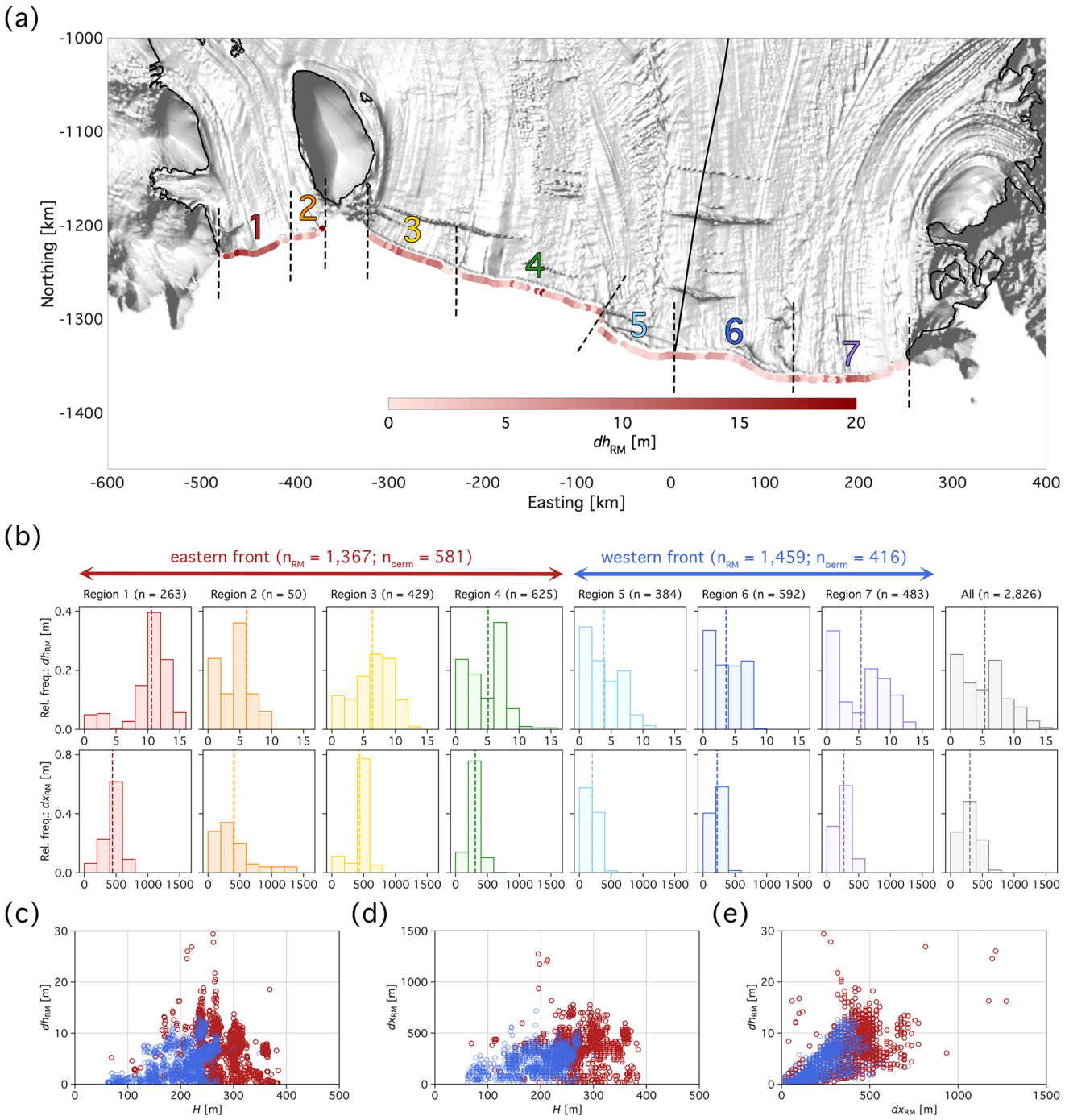

Figure 2. (a) Colored dots show along-front distribution of dh_{RM} (see Figure 1b for definition) from the 2,826 ICESat-2 ATL06 ground track (GT) profiles for which we could identify an R-M structure on the RIS front and compute ice thickness (H), overlaid on a hill-shaded version of the Reference Elevation Model of Antarctica (REMA) mosaic (Howat et al., 2019). GT profiles are for all ICESat-2 cycles (October 2018 to July 2020) available at the time of writing. Dashed black lines across the front indicate boundaries of seven regions used in regional statistical analysis of R-M parameters. Ice-shelf mask and streamline dividing WAIS from EAIS shelf ice are as in Figure 1a. (b) Relative frequency histograms of dh_{RM} (top row) and dx_{RM} (bottom row) for each region defined in (a) and for the entire front ("All"; rightmost column). Dashed vertical lines indicate mean values for each region. Region numbers and numbers of profiles with R-M structures per region (n) are above each column. Arrows at top of (b) specify the eastern (regions 1–4) and western (regions 5–7) portions of the front; numbers of R-M structures and berm-type profiles observed in each portion are indicated. Lower panels provide scatterplots of (c) dh_{RM} versus H, (d) dx_{RM} versus H, and (e) dh_{RM} versus dx_{RM} for all 2,826 GT profiles, color coded red (blue) if they occurred on the eastern (western) portion of the front.

eastern portion, regional histograms of dh_{RM} mostly have peaks and average values greater than 5 m; on the western portion of the front, peaks and averages are typically at values of dh_{RM} below 5 m. There is a similar divide in the distribution of dx_{RM}. Whereas most of the GT profiles that cross the eastern RIS front have dx_{RM} values between 300 and 500 m, GT profiles across the western RIS front mostly have values between 100 and 300 m, resulting in lower regional averages.

We found no evidence of significant changes in R-M statistical characteristics over the October 2018–July 2020 ICESat-2 record. Instead, we interpret the variability of R-M characteristics on scales of a few km along the front (Figure 1d) as evidence that the buoyancy of the bench varies on similar length scales. If so, the spread of dh_{RM} values within a region probably represents the different stages in the life cycles of the R-M structures. Although R-M structures are typically larger in both dh_{RM} and dx_{RM} on the eastern portion of the front, there are R-M structures with small dh_{RM} in all seven regions. Berm structures also occur along the RIS front, but our results suggest that they are more prevalent on the eastern portion of the front (~30% of all GTs) than on the western portion (~22%) (Figure 2b).

4. Discussion

4.1. Drivers of Spatial Patterns in Ice-Front Shape

Prior modeling studies of R-M structures suggest that their spatial scales are determined by ice thickness and ocean properties, and we discuss each of these below.

1. *Ice thickness (*H*)*: We expect from modeling (Mosbeux et al., 2020) that the characteristics of R-M structures depend on H near the ice front (Figures 2c–2d and 3). The observed values of dh_{RM} and dx_{RM} along the RIS front suggest that the distribution of both parameters is at least partially related to H. Near-front H is influenced by mode-3 basal melting (Horgan et al., 2011) and by ice advection, with ice on the eastern portion of RIS (fed by the West Antarctic Ice Sheet) being generally thicker than ice on the western portion of RIS (fed by the East Antarctic Ice Sheet).
   We hypothesize that the relationship between R-M spatial scales and H occurs because a submerged bench of a specified length along the thicker eastern portion of the RIS front will occupy a greater volume than a bench of the same length along the thinner western portion of the RIS front. Assuming ice and ocean density do not vary significantly, this greater volume increases the upward bending moment imparted by the buoyant bench (Figure 1b), which in turn increases dh_{RM}. We expect that dx_{RM} will also be greater for thicker benches, as the bending stiffness of the ice shelf increases with H (e.g., Mosbeux et al., 2020; Wagner et al., 2014). However, the volume of the buoyant bench also has a second-order control on dx_{RM}. The positions of the maximum tensile stress and the moat migrate seaward as the bench grows, converging to a value fixed by the mechanical stiffness of the ice shelf (Mosbeux et al., 2020). Thus, we require additional information about the geometry of the bench to fully characterize the relationship between H and dx_{RM}. The evolution of both dh_{RM} and dx_{RM} may also be related to local rheology and the profile of ice and firn density, as well as preexisting topography associated with rifts (Walker et al., 2021).
2. *Ocean properties*: The principal ocean drivers of bench development are near-surface ocean temperature and surface waves (Kristensen et al., 1982; Scambos et al., 2008). For the southern Ross Sea, measured upper-ocean temperatures are significantly above the freezing point only in summer when sea ice has disappeared (Porter et al., 2019). No direct measurements of surface waves are available along the RIS front, but we expect them to be generally small because sea ice effectively dampens surface waves propagating southward (Horvat et al., 2020), and near-front waves generated by the prevailing northward wind stress across the ice front (Tinto et al., 2019) will be small.

The southern Ross Sea is typically free of sea ice in summer, as the Ross Sea Polynya (Figure 3) expands northward from the ice front beginning in December. The observed mean summertime (December–February) 15% sea ice concentration contour for 1999–2019 (Figure 3), derived from monthly passive microwave data (Meier et al., 2017; Peng et al., 2013), is about 100 km north of the eastern ice front and extends several hundred km farther north in the western Ross Sea. The mean summertime sea surface temperature (SST) from monthly averaged outputs from the fifth generation of the European Centre for Medium-Range Weather Forecasts (ECMWF) Re-Analysis (ERA5; Hersbach et al., 2019) for the same period shows warmer

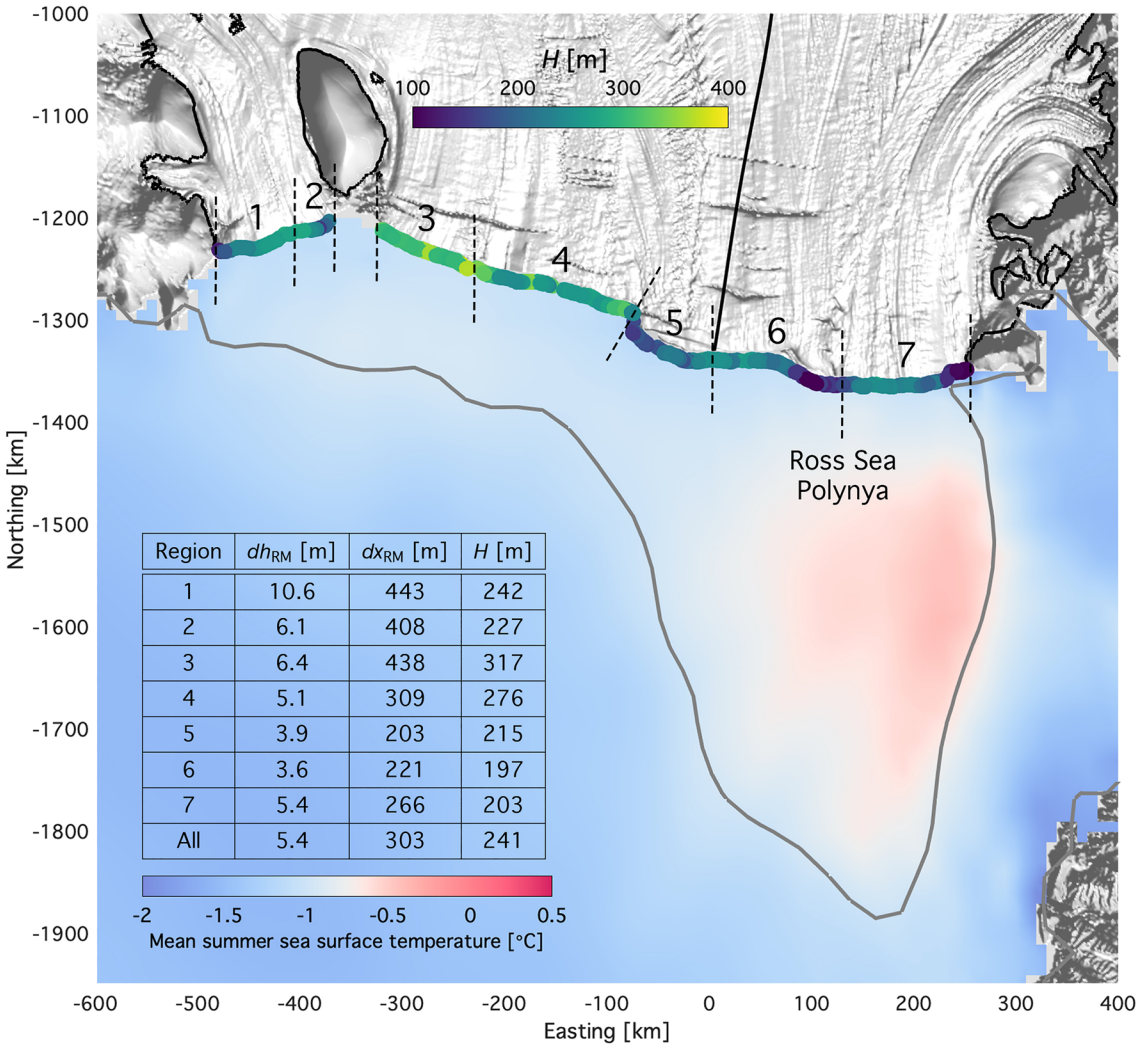

Figure 3. Potential drivers of observed patterns in R-M geometry. Background (hill-shaded REMA mosaic from Howat et al., 2019) shows streaklines delineating ice flow of different glacial units on RIS. The mean summertime SST for the period 1999/2000 to 2018/2019 from Hersbach et al. (2019), extrapolated to meet the RIS front, is shown by blue–red shading. Thick gray line shows the mean summertime 15% sea ice concentration contour (Meier et al., 2017; Peng et al., 2013) for the same period. Ice-shelf thickness (H) 3 km upstream (along track) from the ice front is indicated by the colored dots. Region boundaries are as in Figure 2; ice-shelf mask and streamline dividing WAIS from EAIS shelf ice are as in Figure 1a. The inset table shows mean values of dh_{RM}, dx_{RM}, and H for each region and for the full front ("All").

surface water in the western Ross Sea ~100 km north of the RIS front (Figure 3), but it does not show the relatively warm SSTs close to the front reported by Porter et al. (2019).

These sea ice concentration and SST products suggest that, contrary to our observations (Figure 2), near-front summer ocean and sea ice conditions in the western Ross Sea are more conducive to development of a buoyant bench and R-M growth than in the eastern Ross Sea. We speculate that small-scale ocean processes near the ice front in the eastern Ross Sea lead to development of a more appropriate temperature profile for bench formation (with most ocean heat remaining very close to the ocean surface) than in the western portion, where downwelling of ocean heat, strong mode-3 basal melting (Stewart et al., 2019; Tinto et al., 2019), and mode-3-associated production of cold and fresh meltwater (Malyarenko et al., 2019) might impede the growth of a buoyant bench.

4.2. Implications for Calving

The tensile stress associated with bench-driven bending of the ice shelf, although generally much smaller than the yield stress of pure ice (~1 MPa; Mosbeux et al., 2020), could widen preexisting basal crevasses and ultimately lead to calving, as has been observed at outlet glaciers in Greenland (e.g., James et al., 2014). The environmental conditions, near-surface ocean warming and surface waves, that drive increases in bench buoyancy only occur in austral summer. We speculate that projected changes in summer sea ice (e.g., Bracegirdle et al., 2008; Lenaerts et al., 2016; Massom & Stammerjohn, 2010) could alter both surface warming (Porter et al., 2019) and wave action (Horvat et al., 2020) necessary for bench formation, which in turn would change the relative contribution of R-M-style calving to ice-shelf mass loss. We note, however, that conditions favorable for increased bench formation may also drive mode-3 basal melting (Jacobs et al., 1992; Stewart et al., 2019), such that the interplay of both processes is likely to determine the total rate of mass loss along the ice front.

5. Summary and Outlook

We have used surface elevation data from NASA's ICESat-2 laser altimeter to map rampart-moat (R-M) structures along the front of RIS. These structures are driven by ice flexure due to excess buoyancy from submerged benches of ice that form along the front as warm near-surface water and surface waves create notches in the ice face near the waterline, leading to collapse of the overhanging aerial ice front. We propose that bending stresses acting on preexisting crevasses can lead to calving of small-scale sliver icebergs, contributing to net mass loss from Antarctic ice shelves. Climate-forced changes in this mechanism of mass loss would alter the distribution of freshwater input to the upper ocean in the Ross Sea, and may influence the rate of grounded-ice loss in the Ross Sea sector if the changes occur in regions of high buttressing, such as the area east of Ross Island (Fürst et al., 2016; Reese et al., 2018). Ice-shelf fronts, which advance at rates of order 1 km a^{-1}, also provide a relatively stationary environment for repeat observations of the R-M formation process, which appears to be critical to the destruction of large drifting icebergs, affecting the distribution of glacial meltwater input into the Southern Ocean (England et al., 2020).

Although we focused here on the RIS front, R-M structures exist on other large Antarctic ice shelves, such as the Filchner-Ronne and Amery, where summer environmental conditions are conducive to bench development. Ultimately, improved understanding and quantification of R-M-driven calving will involve a combination of new observations of subsurface ice-front shape (Fried et al., 2015; Orheim, 1987) and time-varying upper-ocean temperature profiles, additional high-resolution elevation and ice-thickness data from the ongoing ICESat-2 mission and CryoSat-2 (Wuite et al., 2019), and observation-based improvements to ice-shelf models that incorporate the reduced yield stress associated with preexisting crevasses.

As the ICESat-2 mission progresses, its data will provide insight into the temporal evolution of R-M structures, including the timescale of development, potential calving, and redevelopment, across all ice shelves. This information will be critical for quantifying the relative contribution of the R-M mechanism to the overall calving flux and for predicting how this contribution might change in a warming Southern Ocean.

Data Availability Statement

ICESat-2 Version 3 ATL03 (https://nsidc.org/data/atl03) and ATL06 (https://nsidc.org/data/atl06) data are available at NSIDC. The Python code for data download and the MATLAB code for front and R-M structure detection are available via Zenodo: http://doi.org/10.5281/zenodo.4697517. The authors acknowledge the use of imagery from the NASA Worldview application (https://worldview.earthdata.nasa.gov), part of the NASA Earth Observing System Data and Information System, and elevation data from the Reference Elevation Model of Antarctica (http://data.pgc.umn.edu/elev/dem/setsm/REMA/mosaic/). Sea ice concentration data are from the NOAA/NSIDC Climate Data Record of Passive Microwave Sea Ice Concentration, Version 3 (https://nsidc.org/data/g02202/versions/3). The authors obtained ERA5 monthly averaged reanalysis outputs of SST, for the years 1999–2019, from modified Copernicus Climate Change Service information (2020; https://cds.climate.copernicus.eu/cdsapp#!/dataset/reanalysis-era5-single-levels-month-

ly-means); neither the European Commission nor ECMWF is responsible for this use of the Copernicus information and component data.

Acknowledgments
The authors thank the OpenAltimetry team for their assistance in accessing data and the ICESat-2 Science Team, particularly the Land Ice group, for their input on the interpretation of ICESat-2 data near ice fronts. The authors are grateful to Brooke Medley for sharing the updated values of H_{fac} from the GSFC-FDM v1 simulations. The authors also thank the editor and two anonymous reviewers for their constructive comments on earlier versions of this manuscript. This study was funded by NASA grants 80NSSC20K0977, NNX17AG63G, and NNX17AI03G and by NSF grants 1443677 and 1443498.

References

Adusumilli, S., Fricker, H. A., Medley, B., Padman, L., & Siegfried, M. R. (2020). Interannual variations in meltwater input to the Southern Ocean from Antarctic ice shelves. *Nature Geoscience*, *13*, 616–620. https://doi.org/10.1038/s41561-020-0616-z

Andersen, O., Knudsen, P., & Stenseng, L. (2015). The DTU13 MSS (mean sea surface) and MDT (mean dynamic topography) from 20 years of satellite altimetry. In Jin, S. (Ed.), & Barzaghi, R. (Eds.), IGFS 2014, International Association of Geodesy Symposia (Vol. 144, p. 111–120). Springer International Publishing. https://doi.org/10.1007/1345_2015_182

Bracegirdle, T. J., Connolley, W. M., & Turner, J. (2008). Antarctic climate change over the twenty first century. *Journal of Geophysical Research*, *113*, D03103. https://doi.org/10.1029/2007jd008933

Bromirski, P. D., Sergienko, O. V., & MacAyeal, D. R. (2010). Transoceanic infragravity waves impacting Antarctic ice shelves. *Geophysical Research Letters*, *37*(2), L02502. https://doi.org/10.1029/2009gl041488

Brunt, K. M., Neumann, T. A., & Smith, B. E. (2019). Assessment of ICESat-2 ice sheet surface heights, based on comparisons over the interior of the Antarctic ice sheet. *Geophysical Research Letters*, *46*, 13072–13078. https://doi.org/10.1029/2019gl084886

Brunt, K. M., Okal, E. A., & MacAyeal, D. R. (2011). Antarctic ice-shelf calving triggered by the Honshu (Japan) earthquake and tsunami, March 2011. *Journal of Glaciology*, *57*(205), 785–788. https://doi.org/10.3189/002214311798043681

Depoorter, M. A., Bamber, J. L., Griggs, J. A., Lenaerts, J. T. M., Ligtenberg, S. R. M., van den Broeke, M. R., & Moholdt, G. (2013). Calving fluxes and basal melt rates of Antarctic ice shelves. *Nature*, *502*, 89–92. https://doi.org/10.1038/nature12567

England, M. R., Wagner, T. J., & Eisenman, I. (2020). Modeling the breakup of tabular icebergs. *Science Advances*, *6*(51), eabd1273. https://doi.org/10.1126/sciadv.abd1273

Fricker, H. A., Young, N. W., Allison, I., & Coleman, R. (2002). Iceberg calving from the Amery ice shelf, East Antarctica. *Annals of Glaciology*, *34*, 241–246. https://doi.org/10.3189/172756402781817581

Fried, M. J., Catania, G. A., Bartholomaus, T. C., Duncan, D., Davis, M., Stearns, L. A., et al. (2015). Distributed subglacial discharge drives significant submarine melt at a Greenland tidewater glacier. *Geophysical Research Letters*, *42*(21), 9328–9336. https://doi.org/10.1002/2015gl065806

Fürst, J. J., Durand, G., Gillet-Chaulet, F., Tavard, L., Rankl, M., Braun, M., & Gagliardini, O. (2016). The safety band of Antarctic ice shelves. *Nature Climate Change*, *6*, 479–482. https://doi.org/10.1038/nclimate2912

Greene, C. A., Gwyther, D. E., & Blankenship, D. D. (2017). Antarctic mapping tools for Matlab. *Computers & Geosciences*, *104*(C), 151–157. https://doi.org/10.1016/j.cageo.2016.08.003

Gudmundsson, G. H., Paolo, F. S., Adusumilli, S., & Fricker, H. A. (2019). Instantaneous Antarctic ice sheet mass loss driven by thinning ice shelves. *Geophysical Research Letters*, *46*, 13903–13909. https://doi.org/10.1029/2019gl085027

Hersbach, H., Bell, B., Berrisford, P., Biavati, G., Horányi, A., Muñoz Sabater, J., et al. (2019). *ERA5 monthly averaged data on single levels from 1979 to present*. Copernicus Climate Change Service (C3S) Climate Data Store (CDS). https://doi.org/10.24381/cds.f17050d7

Horgan, H. J., Walker, R. T., Anandakrishnan, S., & Alley, R. B. (2011). Surface elevation changes at the front of the Ross Ice Shelf: Implications for basal melting. *Journal of Geophysical Research*, *116*, C02005. https://doi.org/10.1029/2010jc006192

Horvat, C., Blanchard-Wrigglesworth, E., & Petty, A. (2020). Observing waves in sea ice with ICESat-2. *Geophysical Research Letters*, *47*(10), e2020GL087629. https://doi.org/10.1029/2020gl087629

Howat, I. M., Porter, C., Smith, B. E., Noh, M.-J., & Morin, P. (2019). The reference elevation model of Antarctica. *The Cryosphere*, *13*, 665–674. https://doi.org/10.5194/tc-13-665-2019

Hughes, T. (2002). Calving bays. *Quaternary Science Reviews*, *21*(1–3), 267–282. https://doi.org/10.1016/s0277-3791(01)00092-0

Jacobs, S. S., Helmer, H. H., Doake, C. S. M., Jenkins, A., & Frolich, R. M. (1992). Melting of ice shelves and the mass balance of Antarctica. *Journal of Glaciology*, *38*(130), 375–387. https://doi.org/10.1017/s0022143000002252

James, T. D., Murray, T., Selmes, N., Scharrer, K., & O'Leary, M. (2014). Buoyant flexure and basal crevassing in dynamic mass loss at Helheim Glacier. *Nature Geoscience*, *7*, 593–596. https://doi.org/10.1038/ngeo2204

Joughin, I., & MacAyeal, D. R. (2005). Calving of large tabular icebergs from ice shelf rift systems. *Geophysical Research Letters*, *32*, L02501. https://doi.org/10.1029/2004gl020978

Kristensen, M. (1983). Iceberg calving and deterioration in Antarctica. *Progress in Physical Geography: Earth and Environment*, *7*(3), 313–328. https://doi.org/10.1177/030913338300700301

Kristensen, M., Squire, V. A., & Moore, S. C. (1982). Tabular icebergs in ocean waves. *Nature*, *297*(5868), 669–671. https://doi.org/10.1038/297669a0

Lazzara, M. A., Jezek, K. C., Scambos, T. A., MacAyeal, D. R., & van der Veen, C. J. (1999). On the recent calving of icebergs from the Ross Ice Shelf. *Polar Geography*, *23*(3), 201–212. https://doi.org/10.1080/10889379909377676

Lenaerts, J. T. M., Vizcaino, M., Fyke, J., van Kampenhout, L., & van den Broeke, M. R. (2016). Present-day and future Antarctic ice sheet climate and surface mass balance in the Community Earth System Model. *Climate Dynamics*, *47*, 1367–1381. https://doi.org/10.1007/s00382-015-2907-4

Liu, Y., Moore, J. C., Cheng, X., Gladstone, R. M., Bassis, J. N., Liu, H., et al. (2015). Ocean-driven thinning enhances iceberg calving and retreat of Antarctic ice shelves. *Proceedings of the National Academy of Sciences of the United States of America*, *112*(11), 3263–3268. https://doi.org/10.1073/pnas.1415137112

MacAyeal, D. R., Okal, E. A., Aster, R. C., Bassis, J. N., Brunt, K. M., Cathles, L. M., et al. (2006). Transoceanic wave propagation links iceberg calving margins of Antarctica with storms in tropics and Northern Hemisphere. *Geophysical Research Letters*, *33*, L17502. https://doi.org/10.1029/2006gl027235

Magruder, L. A., Brunt, K. M., & Alonzo, M. (2020). Early ICESat-2 on-orbit geolocation validation using ground-based corner cube retro-reflectors. *Remote Sensing*, *12*(21), 3653. https://doi.org/10.3390/rs12213653

Malyarenko, A., Robinson, N. J., Williams, M. J. M., & Langhorne, P. J. (2019). A wedge mechanism for summer surface water inflow into the Ross Ice Shelf cavity. *Journal of Geophysical Research: Oceans*, *124*(2), 1196–1214. https://doi.org/10.1029/2018jc014594

Markus, T., Neumann, T., Martino, A., Abdalati, W., Brunt, K., Csatho, B., et al. (2017). The ice, cloud, and land elevation satellite-2 (ICESat-2): Science requirements, concept, and implementation. *Remote Sensing of Environment*, *190*, 260–273. https://doi.org/10.1016/j.rse.2016.12.029

Massom, R. A., & Stammerjohn, S. E. (2010). Antarctic sea ice change and variability - Physical and ecological implications. *Polar Science*, *4*(2), 149–186. https://doi.org/10.1016/j.polar.2010.05.001

Meier, W. N., Fetterer, F., Savoie, M., Mallory, S., Duerr, R., & Stroeve, J. (2017). *NOAA/NSIDC Climate Data Record of Passive Microwave Sea Ice Concentration, Version 3. Southern Hemisphere Monthly Data for December 1999–2018, January 2000–2019, and February 2000–2019*. Boulder, CO: NSIDC: National Snow and Ice Data Center. https://doi.org/10.7265/N59P2ZTG

Mosbeux, C., Wagner, T. J. W., Becker, M. K., & Fricker, H. A. (2020). Viscous and elastic buoyancy stresses as drivers of ice-shelf calving. *Journal of Glaciology*, *66*(258), 643–657. https://doi.org/10.1017/jog.2020.35

Mouginot, J., Scheuchl, B., & Rignot, E. (2017). MEaSUREs Antarctic Boundaries for IPY 2007–2009 from Satellite Radar. In *Version 2. Boundary between West and East Antarctica in IceBoundaries_Antarctica_v02.shp*. NASA National Snow and Ice Data Center Distributed Active Archive Center. https://doi.org/10.5067/AXE4121732AD

Nerem, R. S., Beckley, B. D., Fasullo, J. T., Hamlington, B. D., Masters, D., & Mitchum, G. T. (2018). Climate-change-driven accelerated sea-level rise detected in the altimeter era. *Proceedings of the National Academy of Sciences of the United States of America*, *115*(9), 2022–2025. https://doi.org/10.1073/pnas.1717312115

Neumann, T. A., Brenner, A., Hancock, D., Robbins, J., Saba, J., Harbeck, K., et al. (2020). ATLAS/ICESat-2 L2A Global Geolocated Photon Data. In *Version 3. Region 10 data for Cycle 7 repeat of RGT 0487*. NASA National Snow and Ice Data Center Distributed Active Archive Center. https://doi.org/10.5067/ATLAS/ATL03.003

Neumann, T. A., Martino, A. J., Markus, T., Bae, S., Bock, M. R., Brenner, A. C., et al. (2019). The ice, cloud, and land elevation satellite - 2 mission: A global geolocated photon product derived from the advanced topographic laser altimeter system. *Remote Sensing of Environment*, *233*, 111325. https://doi.org/10.1016/j.rse.2019.111325

Orheim, O. (1987). Evolution of under water sides of ice shelves and icebergs. *Annals of Glaciology.*, *9*, 176–182. https://doi.org/10.3189/s0260305500000574

Peng, G., Meier, W. N., Scott, D. J., & Savoie, M. H. (2013). A long-term and reproducible passive microwave sea ice concentration data record for climate studies and monitoring. *Earth System Science Data*, *5*, 311–318. https://doi.org/10.5194/essd-5-311-2013

Porter, D. F., Springer, S. R., Padman, L., Fricker, H. A., Tinto, K. J., Riser, S. C., & Bell, R. E. (2019). Evolution of the seasonal surface mixed layer of the Ross Sea, Antarctica, observed with autonomous profiling floats. *Journal of Geophysical Research: Oceans*, *124*(7), 4934–4953. https://doi.org/10.1029/2018jc014683

Reeh, N. (1968). On the calving of ice from floating glaciers and ice shelves. *Journal of Glaciology*, *7*(50), 215–232. https://doi.org/10.3189/s0022143000031014

Reese, R., Gudmundsson, G. H., Levermann, A., & Winkelmann, R. (2018). The far reach of ice-shelf thinning in Antarctica. *Nature Climate Change*, *8*, 53–57. https://doi.org/10.1038/s41558-017-0020-x

Rignot, E., Jacobs, S., Mouginot, J., & Scheuchl, B. (2013). Ice-shelf melting around Antarctica. *Science*, *341*(6143), 266–270. https://doi.org/10.1126/science.1235798

Rignot, E., Mouginot, J., & Scheuchl, B. (2017). MEaSUREs InSAR-based Antarctica ice velocity map. In *Version 2. All velocity component data for Ross Ice Shelf*. NASA National Snow and Ice Data Center Distributed Active Archive Center. https://doi.org/10.5067/D7GK8F5J8M8R

Robin, G. D. Q. (1979). Formation, flow, and disintegration of ice shelves. *Journal of Glaciology*, *24*(90), 259–271. https://doi.org/10.3189/s0022143000014787

Scambos, T. A., Bohlander, J. A., Shuman, C. A., & Skvarca, P. (2004). Glacier acceleration and thinning after ice shelf collapse in the Larsen B embayment, Antarctica. *Geophysical Research Letters*, *31*, L18402. https://doi.org/10.1029/2004gl020670

Scambos, T., Ross, R., Bauer, R., Yermolin, Y., Skvarca, P., Long, D., et al. (2008). Calving and ice-shelf break-up processes investigated by proxy: Antarctic tabular iceberg evolution during northward drift. *Journal of Glaciology*, *54*(187), 579–591. https://doi.org/10.3189/002214308786570836

Scambos, T., Sergienko, O., Sargent, A., MacAyeal, D., & Fastook, J. (2005). ICESat profiles of tabular iceberg margins and iceberg breakup at low latitudes. *Geophysical Research Letters*, *32*, L23S09. https://doi.org/10.1029/2005gl023802

Scheick, J., et al. (2019). *icepyx: Python tools for obtaining and working with ICESat-2 data*. National Snow & Ice Data Center. https://github.com/icesat2py/icepyx

Shepherd, A., Ivins, E., Rignot, E., Smith, B., van den Broeke, M., Velicogna, I., et al. (2018). Mass balance of the Antarctic ice sheet from 1992 to 2017. *Nature*, *558*, 219–222. https://doi.org/10.1038/s41586-018-0179-y

Smith, B., Fricker, H. A., Gardner, A., Siegfried, M. R., Adusumilli, S., Csathó, B. M., et al. (2020). *ATLAS/ICESat-2 L3A land ice height, Version 3. All data available for Cycles 1–8 and subsetted between 77°S and 78.9°S and 163.5°E and 157.5°W*. Boulder, CO: NASA National Snow and Ice Data Center Distributed Active Archive Center. https://doi.org/10.5067/ATLAS/ATL06.003

Smith, B., Fricker, H. A., Gardner, A. S., Medley, B., Nilsson, J., Paolo, F. S., et al. (2020). Pervasive ice sheet mass loss reflects competing ocean and atmosphere processes. *Science*, *368*(6496), 1239–1242. https://doi.org/10.1126/science.aaz5845

Smith, B., Fricker, H. A., Holschuh, N., Gardner, A. S., Adusumilli, S., Brunt, K. M., et al. (2019). Land ice height-retrieval algorithm for NASA's ICESat-2 photon-counting laser altimeter. *Remote Sensing of Environment*, *233*, 111352. https://doi.org/10.1016/j.rse.2019.111352

Stewart, C. L., Christoffersen, P., Nicholls, K. W., Williams, M. J. M., & Dowdeswell, J. A. (2019). Basal melting of Ross Ice Shelf from solar heat absorption in an ice-front polynya. *Nature Geoscience*, *12*, 435–440. https://doi.org/10.1038/s41561-019-0356-0

Thomas, R. H. (1979). Ice shelves: A review. *Journal of Glaciology*, *24*(90), 273–286. https://doi.org/10.1017/s0022143000014799

Tinto, K. J., Padman, L., Siddoway, C. S., Springer, S. R., Fricker, H. A., Das, I., et al. (2019). Ross Ice Shelf response to climate driven by the tectonic imprint on seafloor bathymetry. *Nature Geoscience*, *12*, 441–449. https://doi.org/10.1038/s41561-019-0370-2

Wagner, T. J. W., Wadhams, P., Bates, R., Elosegui, P., Stern, A., Vella, D., et al. (2014). The "footloose" mechanism: Iceberg decay from hydrostatic stresses. *Geophysical Research Letters*, *41*, 5522–5529. https://doi.org/10.1002/2014gl060832

Walker, C. C., Becker, M. K., & Fricker, H. A. (2021). A high resolution, three-dimensional view of the D-28 calving event from Amery ice shelf with ICESat-2 and satellite imagery. *Geophysical Research Letters*, *48*, e2020GL091200. https://doi.org/10.1029/2020gl091200

Wuite, J., Nagler, T., Gourmelen, N., Escorihuela, M. J., Hogg, A. E., & Drinkwater, M. R. (2019). Sub-annual calving front migration, area change and calving rates from swath mode CryoSat-2 altimetry, on Filchner-Ronne ice shelf, Antarctica. *Remote Sensing*, *11*(23), 2761. https://doi.org/10.3390/rs11232761